Scripta Materialia 178 (2020) 442–446

Contents lists available at ScienceDirect

Scripta Materialia

journal homepage: www.elsevier.com/locate/scriptamat

Phase transformation volume amplitude as a low-cycle fatigue indicator in nickel–titanium shape memory alloys

Harshad M. Paranjape*, Bill Ng, Ich Ong, Lot Vien, Christopher Huntley

Confluent Medical Technologies, Inc. 47533 Westinghouse Drive, Fremont, CA 94539, United States

ARTICLE INFO

Article history:
Received 19 November 2019
Revised 11 December 2019
Accepted 12 December 2019

Keywords:
NiTi
Shape memory alloys
Fatigue
Digital image correlation

ABSTRACT

Transformation-induced plasticity due to the motion of martensite fronts is a key mechanism for damage accumulation during cyclic loading of NiTi shape memory alloys (SMAs). Intuitively, a larger motion of martensite fronts should result in a larger accumulation of defects, and lead to a shorter low-cycle fatigue life. We validate this hypothesis through fatigue tests and surface strain-field measurements. This result is agnostic of the tensile or bending loading mode. We also demonstrate that the fatigue lifetime intrinsically depends on a combination of two factors: The transformation volume amplitude and the number of inclusions interacting with the phase transformation domains.

Superelastic Nickel–Titanium shape memory alloys (NiTi SMAs) are widely used to manufacture medical implants. The appeal of superelastic NiTi for this application comes from its ability to recover large cyclic deformation. This ability itself arises from a reversible martensitic phase transformation that can be induced by stress. While medical implants are expected to offer a long service life, the reversibility of NiTi deformation has certain limits. Thus, durability and fatigue remain topics of continued research in the field of NiTi SMAs. Inelastic deformation phenomena and metallurgical properties of NiTi are two key factors influencing its durability.

Transformation-induced plasticity – an inelastic deformation phenomenon where the motion of phase transformation fronts results in localized slip – is known to be a mechanism of structural and functional fatigue in NiTi [1]. While the mechanism of transformation-induced plasticity operates at the length scale of the local stress-fields at the interface between austenite and twinned martensite correspondence variants [2], it is reasonable to expect that accumulation of damage due to the same mechanism would occur at the macroscopic transformation fronts (i.e., at Lüders bands). Additionally, Sedmák et al. [3] demonstrated that a stress-concentration zone exists on the austenite side of a transformation front, potentially contributing to the damage accumulation. Results in the literature indicate that incremental damage accumulation due to transformation front motion may be contributing to fatigue in NiTi. Various studies have revealed that low-cycle fatigue failures consistently occur at the transformation front or inside the martensitic region during fatigue testing of NiTi strip specimens [4–7]. Past efforts have also shown a correlation between cycles-to-failure (CTF) and various metrics indicative of the extent of phase transformation such as the hysteresis area, the local strain amplitude, and the size of transformed zone [4–6,8]. Zhang and He empirically demonstrated that branched transformation fronts in thicker fatigue-loaded NiTi strips correspond to lower CTF compared to thinner strips without branching fronts, indicating the deleterious effect of a larger transformation front area [9].

Non-metallic inclusion content is a key metallurgical property of NiTi alloys influencing durability. Commercial NiTi is offered in various purity levels. Standard-purity alloys consist of a certain distribution of carbide and oxide inclusions and high-purity alloys (sometimes referred to as extra-low interstitial or ELI) typically consist of smaller or fewer inclusions per unit volume [10]. The high-purity alloys tend to show superior fatigue performance to the standard-purity variants [11,12]. Micromechanically, Kafka et al. analytically demonstrated that the crack incubation period is inversely proportional to the inclusion diameter [13]. Rahim et al. empirically showed that crack propagation rate does not depend on alloy purity, but crack initiation does [14]. Thus, inclusion content appears to play a central role in determining the damage initiation in NiTi. This is intuitive since inclusions can act as stress raisers and lead to localized phase transformation during fatigue loading [15]. Interestingly, Alarcon et al. have shown that the fatigue life decreases before the maximum nominal stress during superelastic fatigue loading reaches the martensitic transformation onset stress value [16].

* Corresponding author.
E-mail addresses: harshad.paranjape@confluentmedical.com, contact@harshadparanjape.com (H.M. Paranjape).

https://doi.org/10.1016/j.scriptamat.2019.12.014

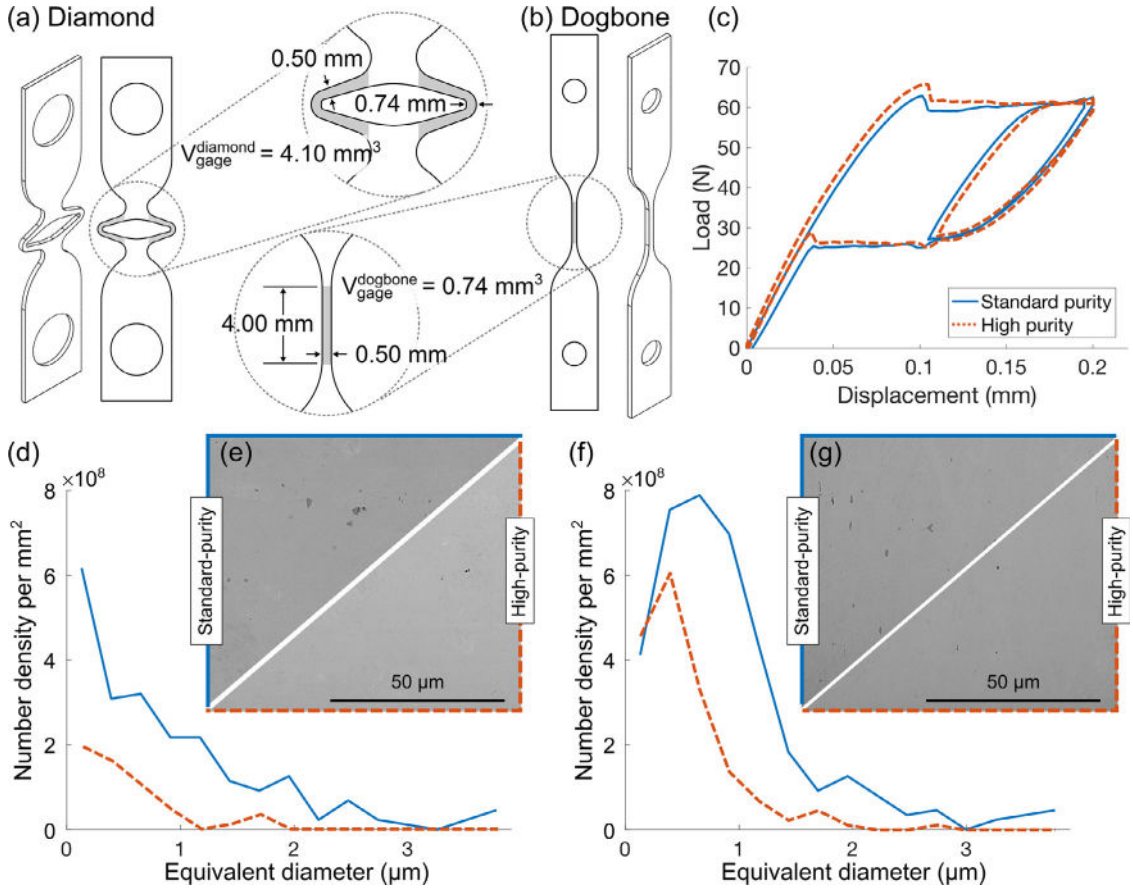

Fig. 1. Specimen description. (a, b) Diamond and dogbone specimen geometries respectively. The gage section is shaded gray and the volume of the gage is annotated. (c) The load-displacement curves at room temperature for a standard-purity dogbone and a high-purity dogbone showing equivalency. (d) Inclusion number density distribution in the transverse cross-section of a standard-purity and a high-purity dogbone. (e) Abridged SEM micrograph showing the inclusion content (dark gray features) in the two materials. Note that the high-purity material has fewer inclusions. (f, g) Corresponding histogram and micrographs for the longitudinal cross-section of the two materials. The legend in (c) applies to (c, d, f). See Supplementary Material for details.

Intuition and the above-mentioned evidence in the literature connecting transformation front motion and inclusion content to the fatigue lifetimes in NiTi led us to pose the following hypotheses. (1) We hypothesize that a larger motion of martensite fronts should result in a larger accumulation of defects, and lead to a shorter low-cycle fatigue life in superelastically loaded NiTi. (2) When the transformation fronts interact with larger or more numerous inclusions, the fatigue lifetimes are worse. We tested these two hypotheses through tensile and fatigue testing of superelastic NiTi.

We manufactured superelastic tensile test specimens with two geometries – dogbone and diamond – as shown in Fig. 1(a, b). When axially stretched, the deformation in the dogbones is primarily uniaxial and in the diamonds, it is bending-dominated. The dogbone specimens were manufactured from NiTi with two different purities: standard-purity and high-purity. These two materials are identical in terms of their thermo-mechanical performance as demonstrated by the equivalent load-displacement curves in Fig. 1(c). However, they differ in terms of the inclusion content. Overall, the high-purity material contains fewer and smaller inclusions as shown by the metallographic cross-sections and inclusion size histograms in Fig. 1(d–g). See Supplementary Material for further details on metallographic inclusion analysis. Thus, three specimen types were prepared: (1) Standard-purity dogbones, (2) high-purity dogbones, and (3) standard-purity diamonds. All specimens were manufactured from superelastic Ti50.8at.%Ni strips using laser-cutting. The specimens were electropolished to remove approximately 30μm material from the surface so as to eliminate any large surface irregularities and the heat affected zone due to the laser cutting process.

We performed tensile tests on the specimens as shown in Fig. 2(a). For the dogbones of each purity, we first applied a pre-extension of 0.2 mm and then applied six subcycle amplitudes of 0.03, 0.06, 0.075, 0.09, 0.105, and 0.12 mm. For the standard-purity diamonds, a pre-extension of 0.5 mm was applied and seven amplitudes of 0.05, 0.1, 0.15, 0.2, 0.25, 0.3, 0.35 mm were applied in the subcycle. We repeated each test on at least two and generally three specimens to obtain a statistics on the deformation. Thus, we performed a total of 54 tensile test cycles. We performed the tests in displacement control at room temperature using a nominal displacement rate of 3.3×10^{-3} mms^{-1}.

We characterized the 2D surface strains in the specimens at the extrema of the tensile subcycle (i.e., points ① and ② in Fig. 2(a)) using digital image correlation (DIC), which is a non-contact and optical technique. An example of the measured strain field at points ① and ② is shown in 2(b, d). We used a Matlab-based computer program to segment the gage area into a low-strain region and a high-strain region. For segmentation, we used a principal strain ($\varepsilon_{principal}$) threshold of 0.015. We defined principal strain as the larger magnitude among $\frac{\varepsilon xx+\varepsilon yy}{2} \pm \sqrt{(\frac{\varepsilon xx-\varepsilon yy}{2})^2 + (\varepsilon xy)^2}$. Here ε_{xx}, ε_{yy}, and ε_{xy} are the axial and shear Green-Lagrangian strains. The high-strain regions furnish the gage area that has undergone austenite to martensite (A $\rightarrow$ M) phase transformation as shown in Fig. 2(c, e). The transformed area is multiplied by the mean specimen width to obtain the transformed volume. The

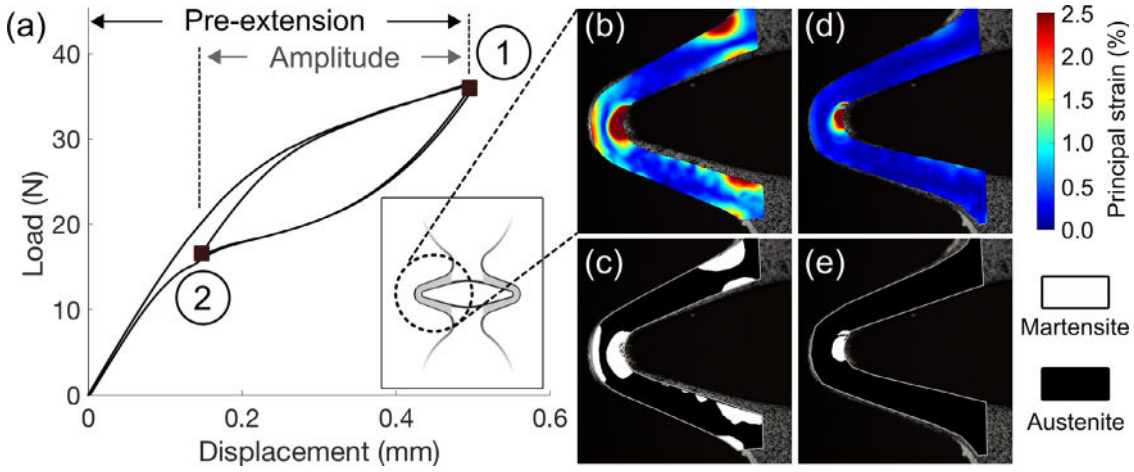

Fig. 2. Segmentation method. (a) The load-displacement curve for a diamond specimen showing the imposed pre-extension and the subcycle amplitude. Points ① and ② denote the extrema of the loading subcycle. (b, d) Gage-section surface principal strain plots at ① and ② respectively obtained using digital image correlation. (c, e) Segmented gage section into an austenitic region and a martensitic region at ① and ② respectively using a strain-based criterion.

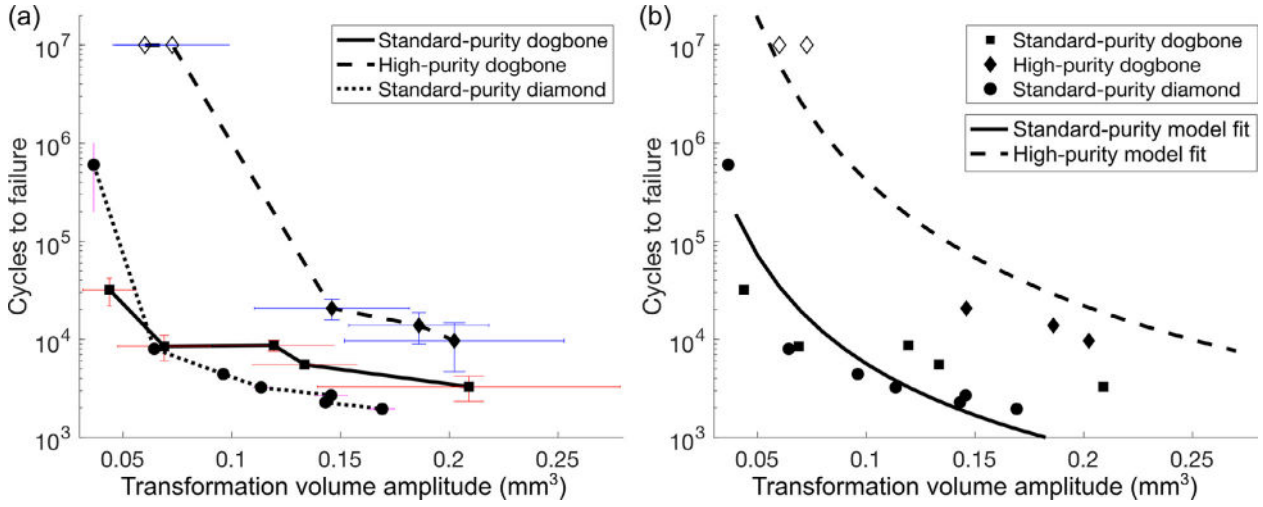

Fig. 3. Results. (a) Experimentally measured cycles-to-failure vs. phase transformation volume amplitude for all specimen types showing an inverse correlation. The filled markers indicate fractures and the empty markers indicate run-out to ten million cycles. The error bars indicate the standard deviation. (b) The same data as in (a) with the fit of a phenomenological model described by Eq. (1).

difference in the transformed volume between the extrema of the subcycle or between points ① and ② furnishes the *phase transformation volume amplitude*. We determined the transformation volume amplitude for all 54 tensile test cycles and then determined the mean and standard deviation of the transformation amplitude for each imposed subcycle displacement amplitude.

We performed fatigue tests on the three specimen types with the identical displacement pre-extension and subcycle amplitude as listed above for the tensile tests. The testing was performed at room temperature in a water bath. At least one and generally three specimens were tested for each amplitude condition. We recorded the CTF for each test and from that determined the mean CTF and the standard deviation CTF for each imposed displacement amplitude. Survival at ten million cycles was considered a run-out. See Supplementary Material for details on the testing methods.

The variation of CTF vs. phase transformation volume amplitude for all specimens is shown in Fig. 3(a). All curves in the figure indicate that the CTF decrease with increasing transformation amplitude. Thus, transformation amplitude is a reasonable low-cycle fatigue indicator. Comparison of the curves for standard-purity dogbone and standard-purity diamond indicates that the results hold for both geometries. That is, the results are agnostic of the axial-dominant vs. bending-dominant nature of the deformation. Comparison of the curves for standard-purity dogbone and high-purity dogbone indicates that the CTF are larger for high-purity material compared to the standard-purity material. These results validate both hypotheses posed above. Larger motion of martensite fronts, quantified in terms of the phase transformation volume amplitude, leads to a shorter low-cycle fatigue life. The fatigue lifetimes are worse when the transformation fronts interact with larger or more numerous inclusions as in the standard-purity material vs. the high-purity material.

We propose a mechanism, schematically shown in Fig. 4, to rationalize these results. Consider a dogbone specimen loaded in tension. In such a specimen, a localized transformation band would form and propagate along the gage length during loading. A localized stress concentration would be present in austenite in the vicinity of such a transformation front as shown in Fig. 4(a) [3]. The inclusions in the NiTi specimen would host their own local stress field. As the transformation front moves, the stress field of the front would superimpose with the stress field of the inclusions that are in the transformation front path. Thus, it is plausible that the superimposed stress field could lead to elevated levels of damage accumulation near the inclusions. As

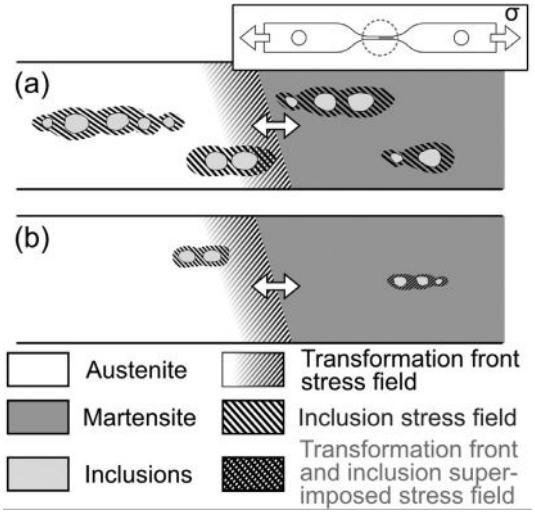

Fig. 4. An illustration of a proposed mechanism relating fatigue life to transformation volume amplitude and inclusion distribution. (a) A transformation front and inclusions in a standard-purity NiTi specimen. (b) A transformation front and inclusions in a high-purity specimen. The inclusions in (b) are fewer and smaller compared to (a).

the transformation front passes through the same collection of inclusions during cyclic loading and unloading, such damage could accumulate and eventually lead to the incubation of a crack and catastrophic fracture. Naturally, larger front motion would lead to a higher fracture probability.

In the case of a similar specimen manufactured from the high-purity NiTi alloy, fewer and smaller inclusions would be present in the gage as shown in Fig. 4(b) and as corroborated by the micrographs in Fig. 1(e, g). Thus, overall, fewer interaction events between a moving transformation front and inclusions would occur, leading to a smaller probability of damage accumulation to a critical level that would cause crack incubation. This rationalizes the relatively longer fatigue life observed in the high-purity dogbones in Fig. 3(a) vs. the standard-purity dogbones.

While explicit Lüders-like bands are not observed in the diamond specimens, under load, the volume of such specimens can still be partitioned into an austenite region and a martensite region. Thus, a similar damage accumulation mechanism as described above would operate in the diamond specimens.

Per the above-mentioned mechanism, the fatigue lifetime (N_F) depends on two factors related to inclusions. CTF inversely correlates to the extreme inclusion size or diameter (D_i) since larger inclusions would produce a stronger stress concentration. CTF inversely correlates to the number density of inclusions (ρ_i). Fatigue lifetime also inversely correlates with the transformation volume amplitude ($\Delta\nu_{PT}$). Thus, a phenomenological expression relating the low-cycle fatigue lifetime to the magnitude of the three factors can be written as

$$\log(N_F) = c(D_i\rho_i)^p(\Delta\nu_{PT})^q. \quad (1)$$

Here c, p, and q are unit-less constants.

We calculated the extreme inclusion diameter by fitting a generalized extreme value distribution [17,18] to the metallographic inclusion number density data shown in Fig. 1(d, f). The extreme diameter was found to be 5.4 μm for the standard-purity material and 3.8 μm for high-purity. We calculated the cumulative inclusion density from the frequency vs. size plots in Fig. 1(d, f). The inclusion density was obtained as $2.231 \times 10^9\,mm^{-2}$ for the standard-purity material and $5.549 \times 10^8\,mm^{-2}$ for high-purity. Based on these values, we obtained the fitting parameters in Eq. (1) as $c = 822.02$, $p = -0.23316$, and $q = -0.37221$. See Supplementary Material for details of these calculations. A fitted model per the parameters determined above is shown in Fig. 3(b). The model reasonably captures the fatigue life of both the standard-purity and high-purity NiTi specimens.

While this work focussed on low-cycle fatigue, cyclic biomechanical processes such as the cardiac rhythm typically subject NiTi implants to fatigue-type loading of relatively small amplitude. Thus, high-cycle fatigue is more relevant in the context of implants. Intuitively, this mechanism would also be applicable in the high-cycle fatigue regime. During high-cycle fatigue, there is essentially no change in the macroscopic transformed volume. However, inclusions still harbor local stress fields that can cause localized transformation and lead to local damage accumulation. This aids in rationalizing the observations of Alarcon et al. [16], who reported that the fatigue life decreases before the maximum nominal stress during superelastic fatigue loading reaches the martensitic transformation onset stress value.

These results could be consequential to the NiTi material purity selection and design of medical implants in various ways. Minimization of phase transformation volume amplitude may be used as an implant design optimization strategy. A higher-purity NiTi alloy with smaller but more numerous inclusions may perform poorer compared to a standard-purity alloy. While this work did not focus on the effects of surface flaws, it is possible that surface flaws larger than a critical size may be detrimental to the fatigue life of a NiTi implant as much as non-metallic inclusions.

This work motivates future efforts directed at the following aspects. Micro-scale characterization studies may elucidate the precise mechanism for damage accumulation and crack incubation around individual inclusions. The dependence of crack incubation and fatigue life on the inclusion-matrix bonding, presence of any voids, and the inclusion aspect ratio may be quantified. The accuracy of the principal-strain-based segmentation process illustrated in Fig. 2 may be verified using a direct transformation volume quantification method such as X-ray diffraction. The mean transformation volume was not controlled in this study and remains a variable worth investigating.

In summary, we introduced a metric – transformation volume amplitude – to quantify the extent of reversible phase transformation during a fatigue cycle. We demonstrated that the fatigue lifetimes in the low-cycle fatigue regime in superelastic NiTi SMA inversely correlate to a combination of two factors: the transformation volume amplitude during a cycle and the number of inclusions interacting with the phase transformation domains. A transformation front + inclusion stress field based mechanism is proposed to rationalize these results.

The authors are grateful to the management at Confluent Medical Technology Inc. for providing resources for this work. HMP would like to thank B. Berg (Boston Scientific), H. Sehitoglu (UIUC), P. Sittner (Czech Academy of Sciences), and C. Bonsignore (Confluent) for comments that influenced this work.

Declaration of Competing Interest

The authors declare that they have no known competing financial interests or personal relationships that could have appeared to influence the work reported in this paper.

Supplementary material

Supplementary material associated with this article can be found, in the online version, at doi:10.1016/j.scriptamat.2019.12.014.

References

[1] D.M. Norfleet, P.M. Sarosi, S. Manchiraju, M.F.-X. Wagner, M.D. Uchic, P.M. Anderson, M.J. Mills, et al., Transformation-induced plasticity during pseudoelastic deformation in NiTi microcrystals, Acta Materialia 57 (12) (2009) 3549–3561, doi:10.1016/j.actamat.2009.04.009.

[2] H.M. Paranjape, M.L. Bowers, M.J. Mills, P.M. Anderson, et al., Acta Materialia 132 (2017) 444–454, doi:10.1016/j.actamat.2017.04.066.

[3] P. Sedmák, J. Pilch, L. Heller, J. Kopeček, J. Wright, P. Sedlák, M. Frost, P. Šittner, et al., Science 353 (6299) (2016) 559–562, doi:10.1126/science.aad6700.

[4] L. Zheng, Y. He, Z. Moumni, et al., Int. J. Solids Struct. 83 (2016) 28–44, doi:10.1016/j.ijsolstr.2015.12.021.

[5] L. Zheng, Y. He, Z. Moumni, et al., Scripta Materialia 123 (2016) 46–50, doi:10.1016/j.scriptamat.2016.05.042.

[6] L. Zheng, Y. He, Z. Moumni, et al., Int. J. Plast. 90 (2017) 116–145, doi:10.1016/j.ijplas.2016.12.008.

[7] D. Catoor, Z. Ma, S. Kumar, J. Mater. Res. (2019) 1–19, doi:10.1557/jmr.2019.254.

[8] Y. Zhang, Y. You, Z. Moumni, G. Anlas, J. Zhu, W. Zhang, et al., Smart Mater. Struct. 28 (6) (2019) 065027, doi:10.1088/1361-665X/ab18b0.

[9] S. Zhang, Y. He, Int. J. Solids Struct. 135 (2018) 233–244, doi:10.1016/j.ijsolstr.2017.11.023.

[10] N. Morgan, A. Wick, J. DiCello, R. Graham, in: Proceedings from the International Conference on Shape Memory and Superelastic Technologies, ASM International, 2006, p. 821.

[11] M. Launey, S.W. Robertson, L. Vien, K. Senthilnathan, P. Chintapalli, A.R. Pelton, et al., J. Mech. Behav. Biomed. Mater. 34 (2014) 181–186, doi:10.1016/j.jmbbm.2014.02.008.

[12] S.W. Robertson, M. Launey, O. Shelley, I. Ong, L. Vien, K. Senthilnathan, P. Saffari, S. Schlegel, A.R. Pelton, et al., J. Mech. Behav. Biomed. Mater. 51 (2015) 119–131, doi:10.1016/j.jmbbm.2015.07.003.

[13] O.L. Kafka, C. Yu, M. Shakoor, Z. Liu, G.J. Wagner, W.K. Liu, et al., JOM 70 (7) (2018) 1154–1158, doi:10.1007/s11837-018-2868-2.

[14] M. Rahim, J. Frenzel, M. Frotscher, J. Pfetzing-Micklich, R. Steegmüller, M. Wohlschlögel, H. Mughrabi, G. Eggeler, et al., Acta Materialia 61 (10) (2013) 3667–3686, doi:10.1016/j.actamat.2013.02.054.

[15] B. Reinholz, S. Brinckmann, Int. J. Fatig. 41 (2012) 72–82, doi:10.1016/j.ijfatigue.2012.01.017.

[16] E. Alarcon, L.e. Heller, S.A. Chirani, P. Šittner, J. Kopeček, L. Saint-Sulpice, S. Calloch, et al., Int. J. Fatig. 95 (2017) 76–89, doi:10.1016/j.ijfatigue.2016.10.005.

[17] M.F. Urbano, A. Cadelli, F. Sczerzenie, P. Luccarelli, S. Beretta, A. Coda, et al., Shap. Mem. Superelasticity 1 (2) (2015) 240–251, doi:10.1007/s40830-015-0016-1.

[18] Y. Murakami, H. Usuki, Int. J. Fatig. 11 (5) (1989) 299–307, doi:10.1016/0142-1123(89)90055-8.

Phase Transformation Volume Amplitude as a Low-cycle Fatigue Indicator in Nickel-Titanium Shape Memory Alloys: Supplementary Material

Harshad M. Paranjape[a,*], Bill Ng[a], Ich Ong[a], Lot Vien[a], Christopher Huntley[a]

[a] *Confluent Medical Technologies, Inc. 47533 Westinghouse Drive, Fremont, CA 94539, United States.*

1. Metallographic Analysis for Inclusion Content Quantification

We performed metallographic analysis on one dogbone specimen manufactured from the standard-purity NiTi material and one dogbone specimen manufactured from the high-purity material. We mounted each dogbone in epoxy and prepared two metallographic samples: one for a transverse cross-section and a second for a longitudinal cross-section. We polished the four samples using silica grinding sheets and diamond slurry. We imaged the samples in an FEI Quanta 200 scanning electron microscope at 2000X magnification. For each cross section, we imaged an area of 135 µm × 640 µm. Examples of cross-section images for the two materials are shown in Figure S1.

We post-processed the image from each cross-section using Matlab software [1]. We binarized each image using adaptive local thresholding. We identified and labeled the inclusion regions using black and white labeling functions in Matlab and determined the equivalent diameter of each identified inclusion assuming a circular cross-section. From the diameter data we created histograms of the size distribution as shown in Figure 1(d, f).

2. Test Methods

We performed tensile testing on the standard-purity dogbones, high-purity dogbones, and standard-purity diamonds using an Instron 5969 load frame with a calibrated 1 kN load cell. We performed the tests in displacement control at room temperature using a nominal displacement rate of 3.3×10^{-3} mm s^{-1}. When tensile testing is performed in air, it is natural for small temperature fluctuations to occur in the specimen gage section due to the exothermic nature of austenite to martensite phase transformation in NiTi. To ensure that the temperature change in the gage is relatively small, we measured the temperature profile in the specimen gage during one typical tensile test using a FLIR T540sc thermal imaging camera. The temperature vs. time profile at the gage center is shown in Figure S2(a). The maximum temperature change was 2.6 °C. This is a relatively small change.

We performed fatigue testing using a five-station Instron ElectroPuls E3000 fatigue tester that was equipped with a stroke transducer and five 125 N load cells. The testing was performed in a water bath maintained at room temperature (21 ± 1 °C). We performed fatigue testing in displacement control at a frequency of 40 Hz. We used the same displacement pre-extension and amplitude in fatigue tests as in the tensile testing. For each test, we recorded the cycles-to-failure (CTF). The diamond specimens have two apices where fracture can occur. We recorded the CTF at the first fracture. The CTF data recorded in this study is listed in Table S1. For most fatigue tests, we used fresh specimens. However, for some fatigue tests, we reused specimens on which one to five tensile test cycles had been performed for the tensile tests

*Corresponding author

Email address: harshad.paranjape@confluentmedical.com (Harshad M. Paranjape)

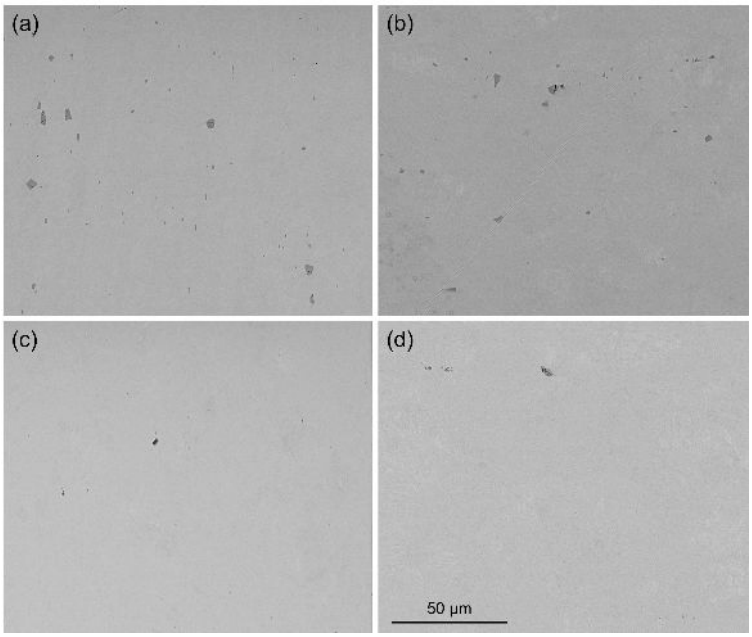

Figure S1: SEM images showing inclusion distribution in the materials. (a) Standard-purity, transverse cross-section. (b) Standard-purity, longitudinal. (c) High-purity, transverse. (d) High-purity, longitudinal. The micron bar applies to all micrographs.

described above. A few tensile test cycles at the same temperature are unlikely to have deleterious effect on subsequent low-cycle fatigue testing.

Considering that the tensile tests and fatigue tests were conducted in different media, we compared the load-displacement curves between the two test methods for some specimens. A comparison of mechanical test data from a tensile test and a fatigue test is shown in Figure S2(b). Apart from some difference in the initial elastic stiffness, the plateau stresses and the load profiles during the subcycle are equivalent between the two test methods.

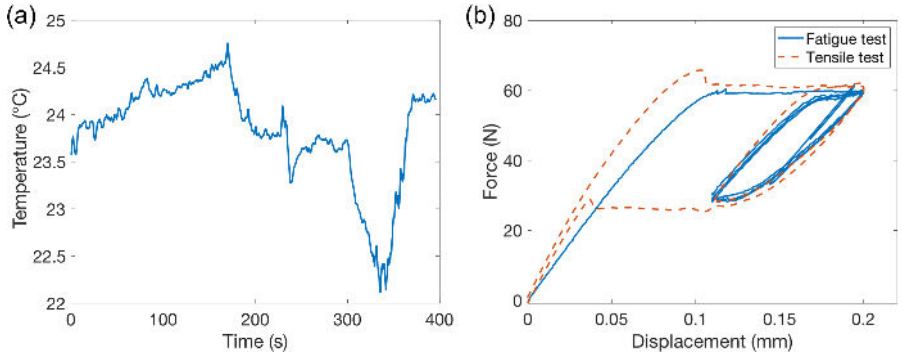

Figure S2: (a) Temperature profile of a point at the center of a dogbone specimen measured using one of the tensile tests. The maximum temperature change is 2.6 °C. (b) Force-displacement curve for a high-purity dogbone from a tensile test and a fatigue test with the same displacement amplitude. The curves are equivalent.

Std-purity Dogbone						
Serial	Pre-extension (mm)	Amplitude (mm)	Mean $\Delta\nu_{PT}$ (mm^3)	Stdev $\Delta\nu_{PT}$ (mm^3)	Mean CTF	Stdev CTF
1	0.200	0.060	0.0442	0.0091	31965	10153
2	0.200	0.075	0.0696	0.0160	8503	2458
3	0.200	0.090	0.1205	0.0206	8692	1113
4	0.200	0.105	0.1350	0.0182	5544	328
5	0.200	0.120	0.2115	0.0522	3287	953
High-purity Dogbone						
Serial	Pre-extension (mm)	Amplitude (mm)	Mean $\Delta\nu_{PT}$ (mm^3)	Stdev $\Delta\nu_{PT}$ (mm^3)	Mean CTF	Stdev CTF
1	0.200	0.060	0.0608	0.0113	10000000*	0
2	0.200	0.075	0.0738	0.0198	10000000*	0
3	0.200	0.090	0.1476	0.0267	20685	4888
4	0.200	0.105	0.1884	0.0241	13861	4871
5	0.200	0.120	0.2050	0.0379	9678	4983
Std-purity Diamond						
Serial	Pre-extension (mm)	Amplitude (mm)	Mean $\Delta\nu_{PT}$ (mm^3)	Stdev $\Delta\nu_{PT}$ (mm^3)	Mean CTF	Stdev CTF
1	0.500	0.050	0.0367	0.0021	602496	402496
2	0.500	0.100	0.0643	0.0006	7999	847
3	0.500	0.150	0.0959	0.0041	4429	0
4	0.500	0.200	0.1136	0.0165	3237	276
5	0.500	0.250	0.1458	0.0281	2686	290
6	0.500	0.300	0.1431	0.0091	2277	255
7	0.500	0.350	0.1692	0.0259	1952	0

Table S1: Transformation volume amplitude and cycles-to-failure raw data. Pre-extension and amplitude are schematically shown in Figure 2(a). $\Delta\nu_{PT}$ refers to the transformation volume amplitude. CTF refers to the cycles-to-failure. Mean and standard deviation (stdev) values reported here are used to plot the errorbars in Figure 3. For CTF, * refers to runout at 10^7 cycles.

3. Transformation Volume Amplitude Determination using Digital Image Correlation

We applied a matte white spray-paint background to the specimens and a speckle pattern consisting of finely-ground charcoal powder. During tensile testing, we photographed the speckle pattern in the gage section surface using a Sony A7III camera with a Mitakon Zhongyi 20 mm f/2 4.5X Super Macro lens. We analyzed the speckle pattern using NCORR DIC software [2] to obtain surface strain components as shown in Figure 2(b, d). From the surface strain components, we calculated the maximum principal strain invariant. At the peak imposed displacement during a tensile test, the principal strain distribution in the gage of a diamond specimen and a dogbone specimen shows a distribution as shown in Figure S3. The strain distribution is bimodal in the case of a dogbone and shows a peak with an elongated tail in the case of a diamond. In NiTi, assuming an upper plateau stress of 400 MPa and an austenite stiffness of 50 GPa, the elastic strain in a dogbone can be estimated to be $400/50000 = 0.008$. Thus, the specimen surface can be partitioned into an austenite region and a martensite region by using a strain based criterion with a segmentation cutoff above approximately 0.008. We used a cutoff of 0.015 in terms of the principal strain magnitude to segment the strain field into two regions. The region with strains above the cutoff may be considered to have transformed to martensite. In Figure S3, the cutoff of 0.015 can be seen to be between the two peaks of the strain distribution in a dogbone specimen. An example of the local strain fields and segmentation into austenite and martensite regions using this method for a dogbone and a diamond specimen

is shown in Figure S4.

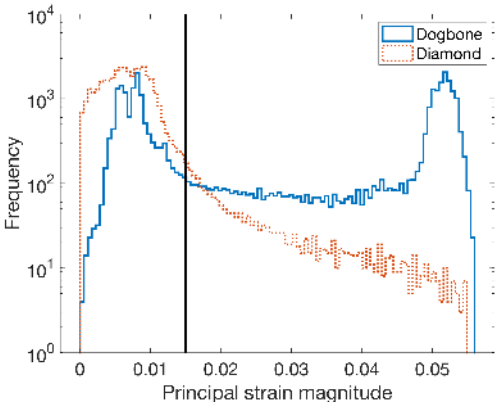

Figure S3: Histogram of principal strain in the gage of a diamond specimen and a dogbone specimen at peak imposed displacement. The segmentation cutoff of 0.015 used to quantify the phase transformation extent is shown by a vertical line.

From the specimen gage surface area that is segmented into austenite and martensite, and assuming that the phase transformation is uniform through the specimen surface, the phase transformation volume can be calculated as the product of the transformed area and the specimen thickness. We define a metric *phase transformation volume amplitude* to quantify the change in the transformed volume during the applied displacement amplitude in a tensile test. This metric is a measure of the movement of transformation zones during cyclic loading. We calculated phase transformation volume amplitude for each tensile test by subtracting the phase transformation volume at (2) from the phase transformation volume at (1) in Figures S4(a, e). From these data, we calculated the mean and the standard deviation of the transformation volume amplitude for each applied displacement amplitude for the diamond and the dogbone specimens. The transformation volume amplitude data calculated in this work is listed in Table S1.

The method described here to measure the phase transformation volume amplitude is segmentation-based. Hence, it is relatively insensitive to small errors in the strain measurement that can occur during 2D DIC testing such as errors due to out-of-plane motion of the test specimen, loss of sharp focus during testing, and environmental thermal fluctuations. In the segmentation scheme, if a principal strain cutoff value different from the one used in this study (cutoff = 0.015) is used, the values of the transformation volume amplitude will change. However, the trends will be maintained.

4. Extreme Inclusion Size Analysis

From the inclusion size distribution data obtained for the standard-purity and high-purity material per the method described in Section 1, we performed analysis to obtain the extreme possible size of an inclusion in the given material. Such analysis needs to be performed, rather than simply using the largest inclusion size in the SEM micrographs, since the SEM metallography analysis samples a finite cross-sectional area of the material and the largest inclusion may be present elsewhere. We followed the method described in general by Urbano et al. [3]. Specifically, we fitted a generalized extreme value distribution function implemented in Matlab [4] to the inclusion distribution data.

The generalized extreme value distribution function y in terms of a shape parameter k (assumed to be 0), location parameter μ, scale parameter σ is defined as

$$y = f(x|k=0,\mu,\sigma) = \frac{1}{\sigma}\exp\left(-\exp\left(-\frac{x-\mu}{\sigma}\right) - \frac{x-\mu}{\sigma}\right). \quad (1)$$

Here, σ and μ are defined in terms of the mean of the inclusion size (diameter) distribution d_{mean} and the

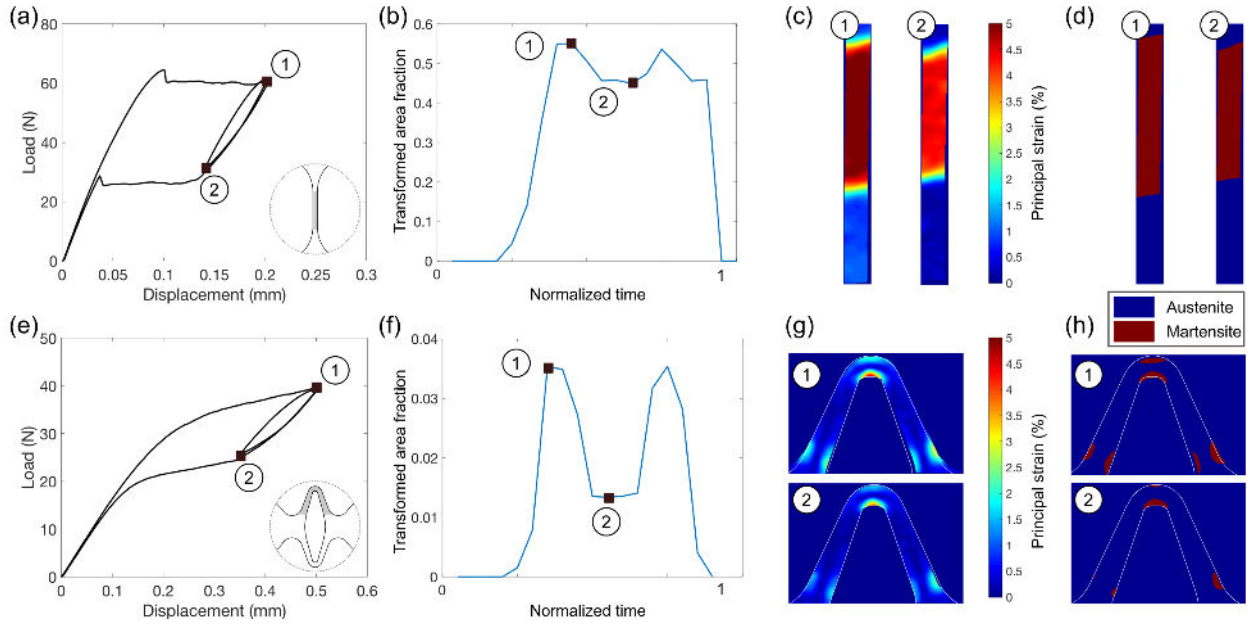

Figure S4: Detailed illustration of the segmentation process. (a) Force-displacement curve for a high-purity dogbone specimen. (b) Martensite area fraction as a function of normalized time during the tensile test. (c) Principal strain field in the gage obtained using DIC. (d) Results of the segmentation process. In (c, d) results at points ① and ② corresponding to those in (a, b) are shown. (e-h) Corresponding illustrations for a diamond specimen. In (a, e) insets, the gage section is highlighted in gray.

standard deviation of the inclusion size distribution d_{stdev} as

$$\sigma = \frac{\sqrt{6}}{\pi} d_{\text{stdev}}, \ \mu = d_{\text{mean}} - \gamma\sigma. \tag{2}$$

Here γ is the Euler's constant and equals 0.5772. d_{mean} and d_{stdev} can be readily computed from the inclusion size distribution data. The extreme inclusion diameter value then, is calculated as the value of this distribution at a given probability p. We calculated the extreme value with $p = 0.999$. Thus, the extreme inclusion size determined here refers to the largest inclusion size that is expected to be present in the given material with a probability of 1 in 1000. The longitudinal data furnished larger extreme diameters for both standard-purity and high-purity materials and thus, is used in these calculations. The extreme diameter was found to be 5.4 µm for the standard-purity material and 3.8 µm for the high-purity material.

5. Phenomenological Low-cycle Fatigue Model Fitting

Per the data in Figure 3 and the mechanism illustrated in Figure 4, the fatigue lifetime (N_{F}) depends on two factors related to inclusions. CTF inversely correlates to the extreme inclusion size or diameter (D_{i}) since larger inclusions would produce a stronger stress concentration. CTF inversely correlates to the number density of inclusions (ρ_{i}). Fatigue lifetime also inversely correlates with the transformation volume amplitude ($\Delta\nu_{\text{PT}}$). Thus, to phenomenologically relate the low-cycle fatigue lifetime to the magnitude of the three factors listed above, we chose the following ansatz for the fitting function.

$$\log(N_{\text{F}}) = c(D_{\text{i}}\rho_{\text{i}})^p(\Delta\nu_{\text{PT}})^q. \tag{3}$$

Here c, p, and q are unit-less constants. We chose a single constant p to relate N_{F} with the extreme inclusion size D_{i} and the inclusion area density ρ_{i} since we tested only two material purities. Thus, fitting more constants to these two parameters may lead to overfitting. In the future, if similar testing is performed on

a variety of NiTi materials differing in terms of inclusion size distribution, then the form of fitting function above may be refined.

We obtained the extreme inclusion size information for this fitting per the method described in Section 4. We calculated the inclusion area density as the total number of inclusions identified through the labeling procedure in Section 1 divided by the area of the metallographic images. We used the raw data for transformation volume amplitude and CTF in Table S1 to determine the unit-less constants c, p, and q using the `nlinfit` nonlinear regression method implemented in Matlab [5].

6. References

[1] Matlab R2018a, The MathWorks, Inc., Natick, Massachusetts, United States, 2018.
[2] J. Blaber, B. Adair, A. Antoniou, Experimental Mechanics 55 (2015) 1105–1122. doi:10.1007/s11340-015-0009-1.
[3] M. F. Urbano, A. Cadelli, F. Sczerzenie, P. Luccarelli, S. Beretta, A. Coda, Shap. Mem. Superelasticity 1 (2015) 240–251. doi:10.1007/s40830-015-0016-1.
[4] MathWorks, Inc., Generalized extreme value distribution, 2019. URL: https://www.mathworks.com/help/stats/generalized-extreme-value-distribution.html.
[5] MathWorks, Inc., nlinfit nonlinear regression, 2019. URL: https://www.mathworks.com/help/stats/nlinfit.html.